Optimisation of an ultrasonic torsion fatigue system for high strength materials

J. Petit, Z. Jiang, O. Polit, T. Palin-Luc

Optimisation of an ultrasonic torsion fatigue system for high strength materials

J. Petit[a,1], Z. Jiang[a], O. Polit[a], T. Palin-Luc[b]

[a] *Laboratoire Energétique Mécanique Electromagnétisme, UPL, Univ. Paris Nanterre 50, rue de Sèvres, 92410 Ville d'Avray, France*
[b] *Arts et Metiers Institute of Technology, CNRS, University of Bordeaux, Bordeaux INP, INRAe, I2M Bordeaux, 33405 Talence, France*

Abstract

The bearable shear stress amplitude in very high cycle fatigue regime (VHCF) is of interest for many applications in mechanics (springs, crankshafts, ball bearings, etc.) when a very high repetition of load cycles occur. This paper proposes to optimise an existing torsion gigacycle fatigue testing system, developed fifteen years ago by the Pr C. Bathias' research team. The aim is to increase the shear stress amplitude applied to the investigated specimen and, consequently, meet the expectations from industries about fatigue life for high strength materials under shear loading. The system differs from other ultrasonic torsion fatigue machines that can be found in the literature, by the combination of two amplification horns, transforming a translation movement into a rotational one. In this work, there are two optimisation objective functions: (i) maximize the shear stress level in the specimen and (ii) minimize the stress level in the fatigue system and mainly in the pin connecting the two horns. The development of the optimised device is essentially carried out by a parametric study and numerical simulations through modal and harmonic analysis. Numerical results are compared with the analytical 1D solution and with experimental results obtained from the new real experimental set-up. Finally, new results in the gigacycle domain are presented concerning the torsion fatigue strength of high strength steels (50CrV4 and 16MnCr5) and discussed.

Keywords: Gigacycle Fatigue, Torsion, Finite Element Analysis, Experimental Set-up, High Strength Steel, Fatigue Shear Stress

[1] Corresponding author. Dr. Johann Petit, Email: johannpetit@parisnanterre.fr

1. Introduction

Up to the end of the last century, the existence of a fatigue limit after a few millions of cycles [1] was accepted by the scientific community. This was the stress amplitude below which fatigue tests lead to no damage in the specimen and its life span was considered as "infinite". This idea could be hardly reconsidered with the technical means available at the time, due to excessive testing time. Today, most of industries still use this fatigue limit concept for designing their components against fatigue failure. However, many mechanical components in engineering machines, such as axles, crankshafts, coil springs, etc., operate at very high numbers of load cycles, until 10^9 or 10^{10} cycles, under stresses lower than the so-called "fatigue limit" and may fracture.

For some decades, new piezoelectric fatigue testing machines were developed [2–5], working at ultrasonic test frequency. In this way, ultrasonic fatigue testing gives access to a time saving method to investigate the fatigue behaviour of materials in the high (HCF) and very high cycle regime (VHCF). Half day becomes enough to perform tests beyond one billion cycles against three years with conventional testing methods. The common function of all piezoelectric systems (or magnetostrictive converters in older investigations [6]) is to make the specimen vibrate at one of its ultrasonic resonance modes, calculated in free-free boundary condition. This latter is required in order to ensure that the global mechanical system naturally vibrates on a resonance frequency. Also, the most stressed section of the specimen has to be large enough and smooth to cause no stress concentration in the material, ensuring to get macroscopic properties without notch effect.

The first ultrasonic fatigue machines were designed for uni-axial tension-compression tests, $R_\sigma = -1$, with R_σ the loading ratio between the minimum and the maximum stress per cycle. Now, different systems can be found to generate different fatigue loadings in the VHCF regime: bending [7, 8], fretting [4, 9], torsion [10–14]. Moreover, superimposition of a mean stress upon the symmetric vibration, by static tensile force or torque load with an additional horn added at the free end of the specimen (see for example [4, 13, 15, 16]), can create a complex cyclic loading with $R_\sigma \neq -1$ and/or multi-axial stress state, increasing the capabilities of this fatigue testing technique. A recent contribution [17] proposes to combine axial/torsion loading using an axial converter with a very special horn.

For all testing configurations, specimens are subjected to cyclic loading at very high frequency. Consequently, in ultrasonic fatigue testing, an important question is the frequency effect on the fatigue behaviour of materials. Mechanical components are typically stressed at low frequencies during actual service. Conventional fatigue testing systems (servo-hydraulic, mechanical, electromagnetic, electrodynamic, etc.) operate at frequencies below $\simeq 300\ Hz$, therefore they can reproduce the real loading frequency more faithfully than ultrasonic fatigue testing. Let us also note that the specimen temperature always increases with the test frequency (variations depend on the intrinsic dissipation of the material and its damping properties), and the resonance frequency may noticeably be affected by the temperature. Fitzka et al. [18] use a system where the loading is not continuous but in a pulse-pause sequence to keep the temperature in a close range for an aluminium alloy 2024-T351. They did not detect any frequency effect under tension-compression fatigue tests, with constant or varying amplitude, but this material presents low self-heating property. Some other tension-compression fatigue tests on different steel grades [19], showing important self-heating properties, revealed some dependency in the evolution of fatigue properties

versus loading frequency.

The knowledge of the material behaviour under cyclic torsion is of great interest, since loading of several technical components is cyclic shear rather than cyclic tension-compression: rolling bearing in many assemblies with rotating movements, drive shafts or gears teeth are typical examples of components subjected to high numbers of torsion load cycles in service. Two kinds of ultrasonic torsion fatigue system can be found in the literature. The first one comprises a converter providing an output angular displacement, a torsion amplifier, named torsion horn, connected to this converter and the specimen designed to vibrate at the resonance frequency of the system. This "direct" system, where the piezoelectric converter directly generates sinusoidal twist oscillations at about 20 kHz, was successfully used to carry out ultrasonic torsion experiments until a shear stress amplitude of 700 MPa on Si-Cr spring steel [13, 20], 850 MPa on carburized SCM420H steel [21] and up to 950 MPa on high-carbon chromium bearing steel [12] while titanium specimens were studied in [22]. The second type of ultrasonic torsion fatigue system is more complex from a mechanical design point of view: a converter, providing an output linear displacement, is connected with a longitudinal horn, itself linked by a pin to a torsion horn, and finally the specimen. From a technological point of view, the second system could reach higher shear stress level in the specimen because linear converters are more powerful than angular ones. That is the reason why we focus on the improvement of this "indirect" system developed by Bathias et al. [11] fifteen years ago. Although the operating of this "indirect" system was validated in [11, 23] to generate shear stress in the material under VHCF regime, this system is not suitable to characterise high strength steels with shear stress amplitude greater than $500 MPa$. Moreover, the stiff connection by the pin between the two horns turns out to be brittle and fails after a few tests.

This paper is dedicated to optimise this ultrasonic torsion fatigue system in order to: (i) largely increase the stress amplitude in the specimen and (ii) increase the robustness of this system. Consequently, the objective of the new "indirect" system presented in this paper is double: from a classic linear piezo-electric converter, the design of the system developed by Bathias et al. is modified in order to test very high strength materials in ultrasonic torsion fatigue, while decreasing stress amplitude in the whole testing system avoiding premature rupture of the set-up during experimental campaigns.

For this purpose, the paper is organised as follow: the next section describes the indirect torsion system, then the optimisation process from parametric study and numerical calculations is presented in the third section. Some explanations about numerical and experimental discrepancies are also exposed using static and transient numerical analysis. Then, the last section is dedicated to the experimental validations and S-N curves determination in gigacycle fatigue regime for two high strength steels are presented.

2. Description of the indirect torsion fatigue system

In order to determine the torsion fatigue strength of metallic alloys up to 10^{10} cycles, an ultrasonic torsion fatigue system (Fig. 1) was originally designed by Marines et al. [11]. The main component of this ultrasonic system is a piezoelectric transducer, which converts an electrical signal at a frequency of 20 kHz into a longitudinal mechanical displacement at the same frequency. The electrical signal is provided by a generator that automatically turns to one of the natural resonance frequency of the system (piezo-electric converter, horn, specimen). In case

of pure fully reversed torsion loading applied to the specimen, the system vibrates on a free-free boundary condition resonant mode. Two horns are attached to the transducer. The first one, named Tension-Compression horn (TC horn), is firmly connected by an axial screw to the converter and amplifies the longitudinal mechanical displacement. The second one, Torsion-Torsion horn (TT horn) is rigidly jointed at the end of the first horn by a radially press fitted pin going through both horns from end to end, see Fig. 1. This TT horn is fixed perpendicularly to the first one, so that it transforms the linear displacement of the longitudinal horn into an angular displacement and can vibrate on its first torsion resonant mode. Thanks to its shape, the TT horn amplifies the angular displacement applying a higher value to the specimen. A torsion fatigue specimen is designed to run in the same resonance as the system at a loading ratio of $R_\sigma = -1$. The specimen is directly attached by a screw at the end of the second horn.

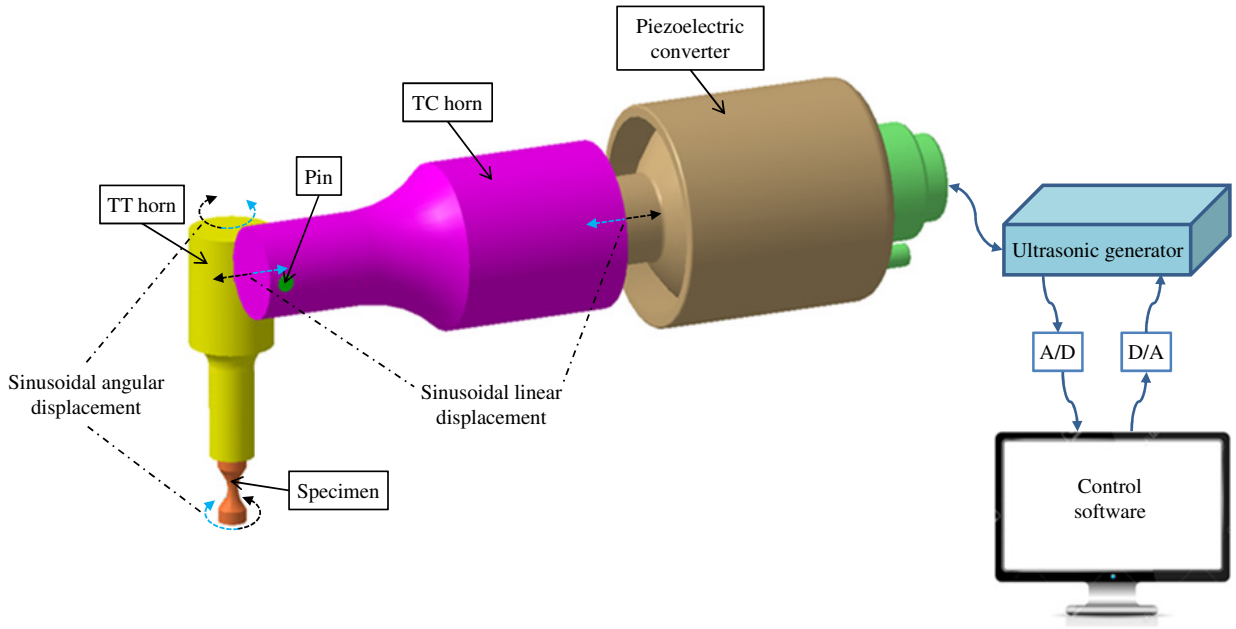

Figure 1: Scheme of the indirect torsion fatigue system designed by Bathias et al. [11]. The straight and curved arrows represent the vibratory motion of the system.

During the vibration of the testing system, the amplitude of the angular displacement reaches its maximum value at both ends of the specimen while the maximum shear strain occurs in the middle section, producing the required high frequency sinusoidal shear stress. The input displacement amplitude at the beginning of the TC horn can be measured by means of a dynamic displacement sensor, like optical fiber or laser sensor, which permits the measurements of the displacement from 1 to 150 μm with a resolution of 0.1 μm. The maximum strain value can be measured directly using miniature strain gauges, positioned at the midsection on the specimen surface. Under elastic behaviour, a linear relationship exists between the input displacement and the strain at the midsection of the specimen. Consequently, the magnification factor of stress, expressed in $MPa/\mu m$, can be calculated according to these measurements, assuming also the proportionality between strain and stress given by the Hookes's law at the macroscopic scale in the gigacycle regime.

The calibration of this experimental set-up is defined as follow: to a given value of the generator input voltage

corresponds an input displacement amplitude of the TC horn and, therefore, a specific maximum shear stress amplitude in the specimen, related to the magnification factor of the system. The matching between the input voltage and the maximum shear stress amplitude does not change as long as there is no evolution of the material properties and the external conditions. A calibration curve is presented in Fig. 2. It can be observed that the relationship between the input voltage and the maximum shear stress is linear. Although the voltage range of the generator belongs to $[-7.5\ V, +10\ V]$, the calibration curve does not exceed $-3\ V$, because of strain gauge connections failure above this value. An in-house software controls the generator to produce the expected shear stress and keeps it constant all along the test. Moreover, if the material properties or testing conditions change during the test, a sensor can be used to measure the rotation at the end of the specimen and this information can be used by the software, to adapt the input voltage in real time recovering the right stress value into the specimen. This is the basic working principle of the torsion fatigue machine used in this study, where amplitude measurement and control are the same as those used for axial ultrasonic fatigue loading [4]. All the other technical details related to the torsion fatigue system, particularly the analytical calculations for the design of the system, have already been published in [3, 10, 11, 24–27] for example.

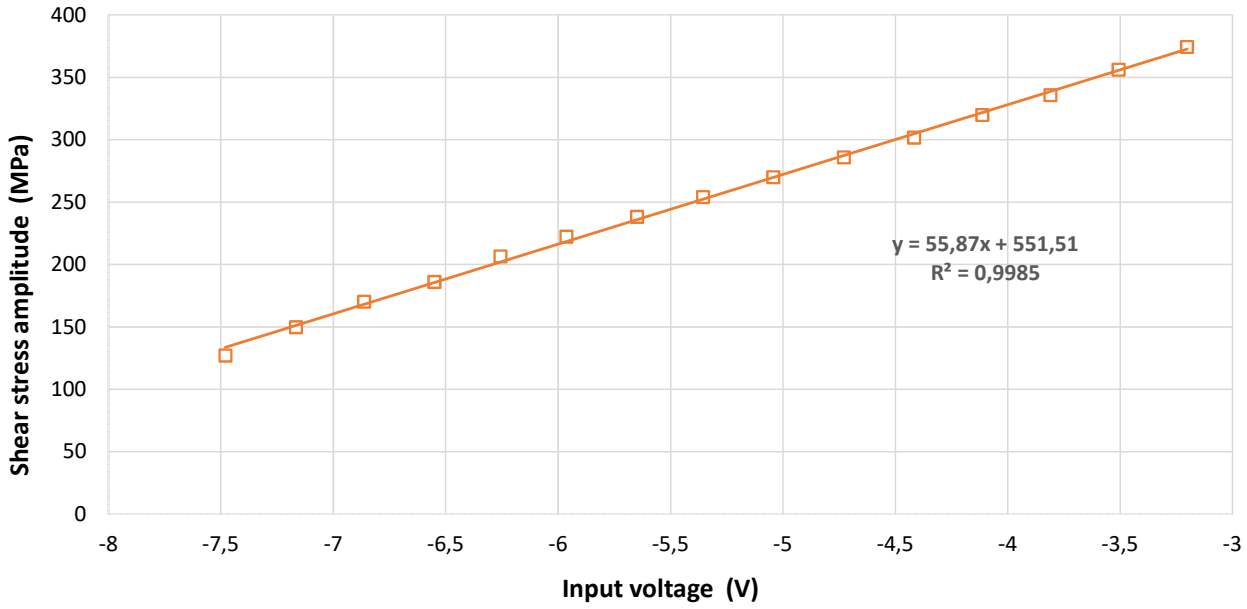

Figure 2: Calibration of the system for a steel specimen: shear stress amplitude at the specimen center against generator input voltage.

In the following, several aspects of the former system are modified in order to noticeably increase the shear stress in the specimen while decreasing stress in the rest of the system. Optimisation procedure is mainly based on numerical calculations because resolution of the analytical problem would become too much complex with the geometrical features modifications considered hereafter. Note that the shear stress amplitude in the specimen can also be increased depending on the specimen geometry, but it is out of the scope of this paper.

3. Optimisation of the indirect torsion fatigue system

Because of the high resistance of high strength materials, such as bearing steels, it is necessary to apply a very high stress amplitude to the specimen in order to determine the S-N curve of such alloys. However, as mentioned previously, in torsion, the shear stress obtained with the original machine developed by Bathias et al. [11] is too small for this purpose. Consequently, a new optimised version of the original ultrasonic torsion system has to be designed. In the former version, the connection between the two horns by a radial pin, which is mainly loaded in bending, was weak and premature failures were observed. The stress amplitude inside this connection has to be decreased. So, two opposite objective functions in this optimisation problem rise: (i) the optimised system must provide a higher shear stress amplitude in the specimen; (ii) it has to lead to a lower stress at the horns connection.

Moreover, the optimization will be done only for a given specimen geometry. The chosen geometry is smooth for having a theoretical stress concentration factor close to the unity. A new design of the specimen geometry may introduce stress concentration in the central part of the specimen. This is not the aim of this work. In such case, the torsion properties would be altered by the notch effect.

3.1. Experimental set-up components

The components of the original ultrasonic system are: the two magnifying horns (TT and TC) and the pin connection. To increase the shear stress amplitude in the specimen, the angular displacement at the end of the specimen has to be increased. At the resonance, it can be easily checked that the relationship between the longitudinal input displacement of the TC horn and the angular displacement at the end of the specimen is linear. The first idea to increase the shear stress in the specimen could be to increase the input displacement of the TC horn. However, increasing this value would lead to failure because the stress in the pin would be also higher. Consequently, modifications of the global system must be introduced. In particular, the magnification factor can essentially be increased by designing a new TT horn. In order to decrease the stress in the pin, one could change the material or some geometrical features of the system. The material used for the pin in the first version of the torsion fatigue system is a QT (Quenched and Tempered) 100CrMo6 steel with a very high mechanical strength (UTS = 1800 MPa and $Hardness$ = 55 HRc) ; it has been decided to keep it. Thus, optimisation mainly concerns the modification of some geometrical characteristics of the system: pin radius, chamfers at the connection of the two horns, bore in the horns and modification of the TT horn dimensions. A sketch of the new version of the indirect torsion fatigue system proposed in this paper is illustrated in Fig. 3. The choice of the different new design parameters is detailed in the following.

3.2. Parametric study for optimisation of the new system

All simulations carried out in this study are performed by Finite Element Method (FEM), using ANSYS® commercial software. The geometry of the numerical model is based on the drawing of Fig. 3. It consists of the two horns (TC and TT), the pin and the specimen. The components have been modeled without contact but with perfect displacement continuity at the interfaces between components. Materials used are TA6V titanium

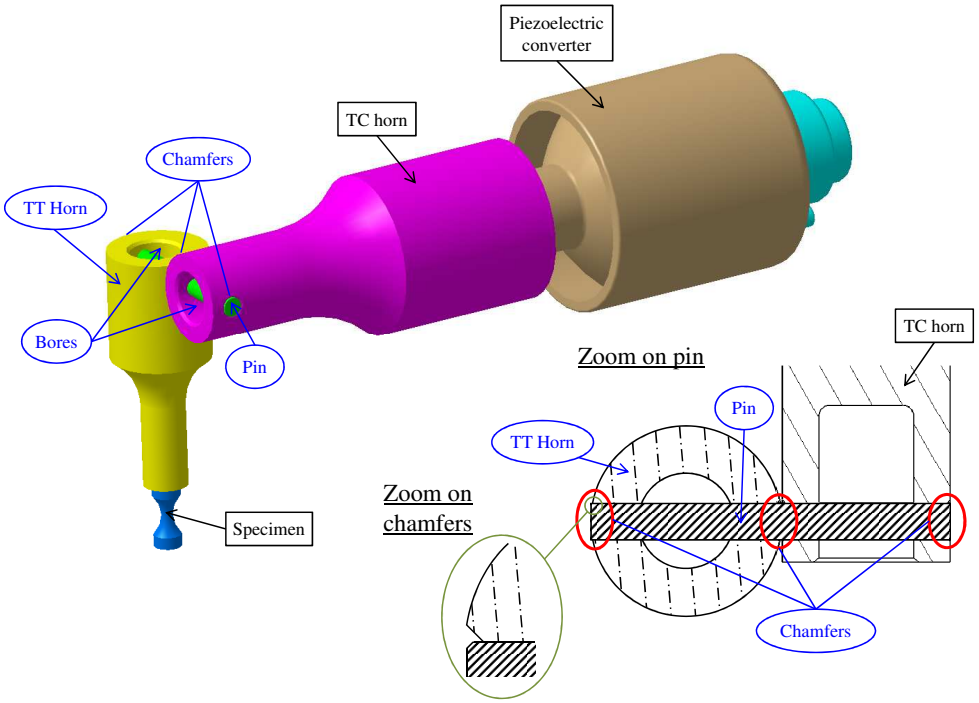

Figure 3: Sketch of the new version of the indirect torsion fatigue system: the parts to be optimised are enclosed by ellipses.

alloy for the horns and 100CrMo6 QT steel for the pin and the specimen. These materials are assumed to be isotropic with a linear elastic behaviour at the macroscopic scale. Two types of analysis are required to determine the stresses in the system. First, a modal analysis gives the resonance frequencies of the system. One modal frequency must be close to 20 kHz with a margin $\pm 500Hz$. Second, a harmonic analysis is performed to deduce displacements, strains and stresses in the system under the resonant frequency. For this second analysis, a sinusoidal longitudinal input displacement with an amplitude of 1 μm is imposed as kinematic boundary condition on the large face of the TC horn (screwed to the converter).

The approach adopted in the next paragraphs to carry out the optimisation of the torsion fatigue system is as follows: the results of the geometric modifications are compared with the performances of the original system while keeping independence between all design parameters. Indeed, it could be demonstrated that correlation between the design parameters is low, allowing an easy interpretation of the results when varying the parameters one by one.

3.2.1. Dimensions of the TT horn

The first and main parameters to increase the shear stress amplitude in the specimen while decreasing stress level in the system, are related to the TT horn geometry, presented in Fig. 4. Tab. 1 proposes several models of the TT horn: the original one (model 1), three versions with various radius R_g of the large cylindrical part (models 2 to 4) and two other versions with various length L_v of the intermediate part with progressive section (models 5 and 6). When varying one of the three parameters R_g, R_p or L_v, the length L_p or the length L_g has necessarily to be adapted for resonance requirement. Then, the total length L_t of the horn is also changed. L_t is given in Tab. 1. Considering the null tangent at the beginning of the intermediate part (after the small cylinder

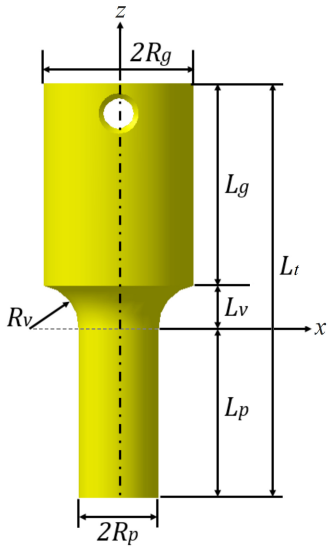

Figure 4: Geometry and parameters of the TT horn.

part), the fillet radius R_v can be easily deduced from the three other geometric parameters by the following equation:

$$R_v = \frac{L_v^2}{2(R_g - R_p)} + \frac{R_g - R_p}{2} \tag{1}$$

The magnification factor of the system is proposed as comparative index between the different models. It can be observed that the higher the ratio between the large and the small radius, the higher the magnification factor and, consequently, the shear stress in the specimen. According to the results from models 4 to 6, the variation of the progressive section in the intermediate part of the TT horn has nearly no effect on the magnification factor. Nevertheless, a too short intermediate part would lead to premature fatigue failure due to stress concentration. That is why, a longer intermediate part is chosen for the new optimised system.

TT horn	large radius	small radius	progressive section length	fillet radius	total length	modal frequency	magnification factor
Model	R_g (mm)	R_p (mm)	L_v (mm)	R_v (mm)	L_t (mm)	(Hz)	$(MPa/\mu m)$
1 (original)	15	8	8.5	8.7	81.8	19765	115.4
2	16	8	8.5	8.5	82.1	19766	137.0
3	17	8	8.5	8.5	82.3	19742	170.9
4	18	8	8.5	8.6	82.5	19747	200.7
5	18	8	15.0	16.2	86.1	19734	197.5
6	18	8	20.0	25.0	88.9	19733	198.8

Table 1: Comparison of five TT horn models according to their geometrical features. The magnification factor is obtained in the smallest cross section of the specimen.

A first torsion fatigue system made up using a TT horn with $L_v = 12\ mm$ was manufactured. A premature crack was observed at the surface of the progressive section of the TT horn due to the combination between

stress concentration and a not fine enough surface roughness obtained after machining. In order to avoid this problem, it was decided to noticeably increase L_v until 20 mm and to polish the horn. This new system (model 6) turns out much more robust.

3.2.2. Pin radius

The diameter of the pin can be modified in order to decrease the stress level in this component. Tab. 2 shows the influence of the pin radius on the maximum shear stress τ_s^{max} in the middle of the specimen and on the maximum Von Mises equivalent stress $\sigma_{eq,p}^{max}$ in the pin. Then, a "*design ratio*" r_d is defined as folows:

$$r_d = \frac{\tau_s^{max}}{\sigma_{eq,p}^{max}} \tag{2}$$

in order to compare the different configurations of the system; the higher r_d, the better the choice for the optimisation parameters. It can be observed from Tab. 2 that r_d is directly related to the radius of the pin. A pin radius of 4 mm is chosen, because r_d is largely improved with respect to the original design. A larger pin diameter could still increase r_d, but would significantly reduce the displacement amplitude of the specimen, and thus the maximum shear stress τ_s^{max} in the specimen.

pin radius (mm)	modal frequency (Hz)	τ_s^{max} (MPa)	$\sigma_{eq,p}^{max}$ (MPa)	r_d
2.5	19776	118.4	56.7	2.09
3 (original)	19765	115.4	54.1	2.13
3.5	19747	116.7	48.7	2.40
4	19738	115.7	32.8	3.53

Table 2: Influence of the pin radius on the design ratio r_d defined as: maximum shear stress in the specimen/maximum Von Mises equivalent stress in the pin.

3.2.3. Chamfers

In the former design of the ultrasonic torsion fatigue system, it could be noticed that the facture initiation of the pin was often located at the interface of the two horns, starting from the surface of the pin. The pin is press fitted in both horns and the two horns are in contact, during vibrations, involving friction between the pin and the horns. This friction is intensified when the edges of the drilled holes into the horns are sharp, as it is obtained after machining. Therefore, chamfers can be realised in order to reduce the stress concentration between the pin and the horns, by smoothing the drilled edges. The depth of the chamfer is around 1 mm. The effect of the chamfers can be checked numerically and the design ratio r_d is used to analyse the results. Tab. 3 gives the r_d values, when varying chamfers angle while keeping the same depth. It can be interpreted as: the presence of chamfers significantly reduces the Von Mises equivalent stress in the pin for the same shear stress value imposed in the specimen. Very small fluctuation on the modal frequency and on the stress ratio are observed by varying the chamfer angle value. For the sake of technical simplicity, the chamfer angle is chosen equal to 60°.

chamfer angle (mm)	modal frequency (Hz)	r_d
0° (no chamfer)	19937	1.21
45°	19934	1.90
60°	19924	1.92
75°	19926	1.98

Table 3: Influence of the chamfers angle along the edges of the drilling in the TC and TT horns on the design ratio r_d.

3.2.4. Bore in the horns

The original ideas for the bore in horns was to simplify pin assembly through the two horns and to reduce contact and friction between pin and horns. Then, we propose to evaluate the effect of the bore diameter on the Von Mises equivalent stress in the pin. As depicted in Fig. 3, bore concerns the small cylindrical part (with an exterior diameter of 32 mm) of the TC horn and the large cylindrical part (with an exterior diameter of $2R_g = 30$ mm in the original version) of the TT horn. Tab. 4 presents the r_d ratio obtained varying the bore diameter on both horns. It can be observed that a larger diameter increases the ratio but variations are small. Nevertheless, bore with a large diameter provides two other significant advantages: it enables to decrease the mass of the system without changing its vibration properties and to increase heat exchange around the pin. In the optimised version of the system, bore diameters are defined as follow: 16 mm and 18 mm for the TC and the TT horns, respectively. This choice decreases the stress in the pin and keeps the system working. It is also observed that the depth of the cavity has no influence on the stress in the pin as soon as the pin is totally uncovered by the bore. The depth of the bores was chosen at 30 mm.

bore diameter (mm)	modal frequency (Hz)	r_d
0 (without)	19765	2.13
10	19856	2.18
12	19892	2.23
14	19923	2.21
16	19962	2.29

Table 4: Influence of the bore diameter in the horns on the design ratio r_d.

3.2.5. Final design of the optimal system

The optimisation of the different parts of the torsion fatigue system was presented in the previous subsections. The optimal values for the design parameters were obtained from numerical simulation through modal and harmonic analysis performed with the ANSYS® FEM software. A comparison between the former system and the new optimised one is given in Tab. 5 considering all the proposed modifications and steel specimen

with a 210 GPa dynamic modulus. The modal frequencies of the two systems are closed and in the range $[19500\ Hz, 20500\ Hz]$ required by the converter. It can be observed that the magnification factor and the r_d ratio are largely improved in the optimised version. For a given specimen geometry and for the same displacement amplitude imposed by the converter at the top of the specimen, the shear stress amplitude reached in the smallest cross section is quite higher (more than twice) with the optimised system than the original one. Besides, the life span of the pin is considerably increased. Indeed, during all the testing campaign reported in section 6, the pin has never been changed, whereas previously the pin was changed each 5 specimens tested up to 10^9 cycles approximatively. In terms of materials and surface roughness of each component (horns and pin), nothing was changed in the optimised system. The parametric study based only on geometrical considerations (and carried out by numerical analysis) has improved both the performances and the sustainability of the system.

torsion fatigue system	modal frequency (Hz)	magnification factor ($MPa/\mu m$)	r_d
original	19765	115.4	2.13
optimised	19929	232.9	9.49

Table 5: Comparison of the original and optimised systems.

It is also important to check that other modes, in particular bending modes, are outside the working range of the converter. Fig. 5 presents the three modes, a bending one at $18865Hz$, the torsion one at $19929Hz$ and the next bending mode at $20771Hz$. This new system is also optimal as only the torsion mode is in the working range of the converter and no coupling with other vibrational modes may occur during tests.

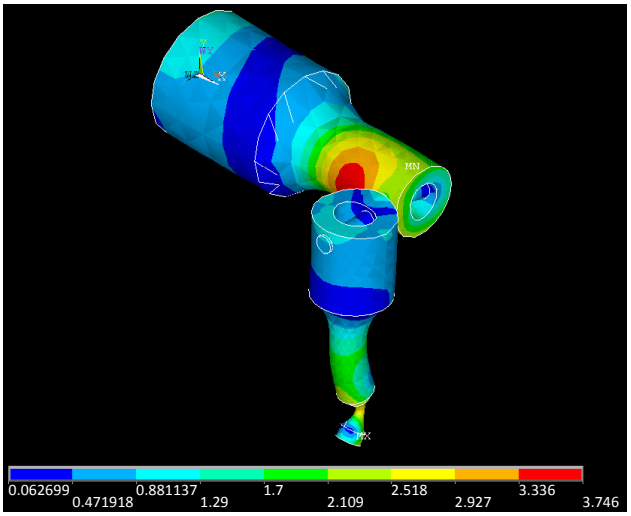

(a) Bending mode: $18658Hz$

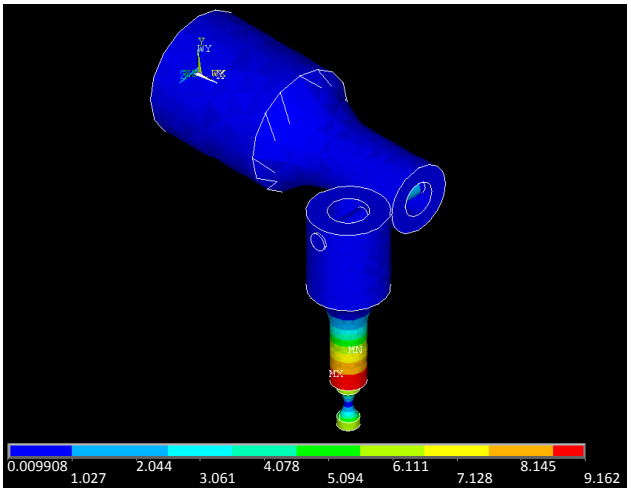

(b) Torsion mode: $19929Hz$

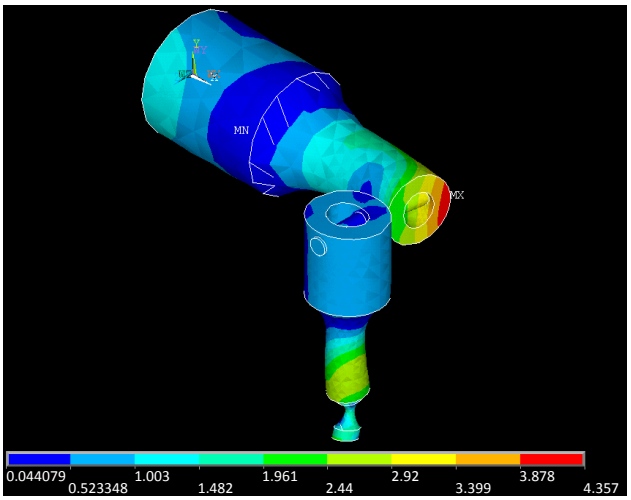

(c) Bending mode: $20771Hz$

Figure 5: Deformed shapes (magnified) of the optimised system obtained by modal analysis: the torsion mode and the two surrounding bending modes.

4. Analytical solution and comparison with FEM analysis

In this section, the profiles of the amplitude of the longitudinal displacement in the TC horn and of the angular displacement in the TT horn and in the specimen are given as a function of the position along their length using a one-dimensional (1D) analytical model. The analytical approach can be found in [26–28] and is applied to each part of the system, separately. Development of equations for the specimen is detailed in Appendix A and the methodology is the same for horns. The 1D analytical solution is obtained by setting resonant frequency, material properties and some geometrical features of the parts, but bores in horns are not taken into account in these 1D models. Then, the total resonant length and displacement/stress evolutions along each part are obtained. These results are compared with the displacements obtained from the FE model of the whole experimental set-up previously defined. In order to compare the results between analytical solution and FE model, the same geometry is used for both approaches. Consequently, the resonant frequency of the analytical solution had to be manually adjusted to obtain the same total length of each component and discrepancies with the resonant frequency of the FE model inevitably arise.

4.1. TC horn

Fig. 6(a) shows the amplitude of the longitudinal displacement evolution along the TC horn axis. Profiles provided by the 1D analytical solution and the FE model are very similar. There is a difference on the resonance frequency (f) of about 500 Hz ($\approx 2.5\%$) because the modal analysis concerns the whole system for FEM while the analytical approach considers the TC horn only. It can be observed that displacement profiles superimposed well, except in the curve part and at the end of the TC horn. This gap between the two approaches is mainly due to the presence of the bore, as mentioned previously, but also to Poisson's ratio effect which arises in the dynamic behaviour of solid structures (FE model), while it is neglected in the 1D analytical approach. To a lesser extent, it can be also related to the description of the curvature of the intermediate part: in the FE model, an arc of circle is used to approximate the exact cosinus hyperbolic profile assumed in the 1D analytic solution. The amplitude difference at the horn end in contact with the TT horn is only 2.5%.

4.2. TT horn

Fig. 6(b) shows the angular displacement evolution along the TT horn axis. Profiles provided by the 1D analytical solution and the FE model are quite similar. It can be observed that the displacement profiles superimpose very well until the middle of the progressive radius part of the TT horn, then the two curves shift from each other and remain parallel. As previously observed for the TC horn, the amplitude at the end of the TT horn is higher for the FE model. The difference between the two analysis arises from the same reasons as set out in the previous paragraph. Nevertheless, the amplitude difference at the horn end in contact with the specimen remains low with a value of 3.8%.

4.3. Specimen

Finally, Fig. 6(c) shows the angular displacement evolution along the specimen axis. Profiles provided by the 1D analytical solution and the FE model are very similar, despite, as for horns, the difference on resonant

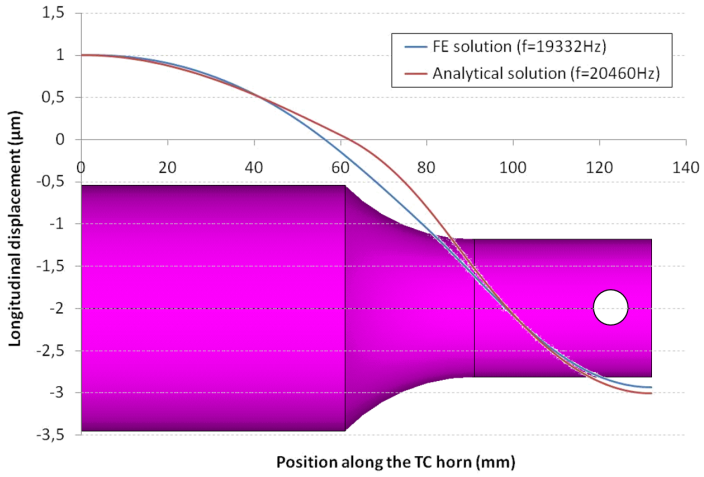

(a) TC Horn

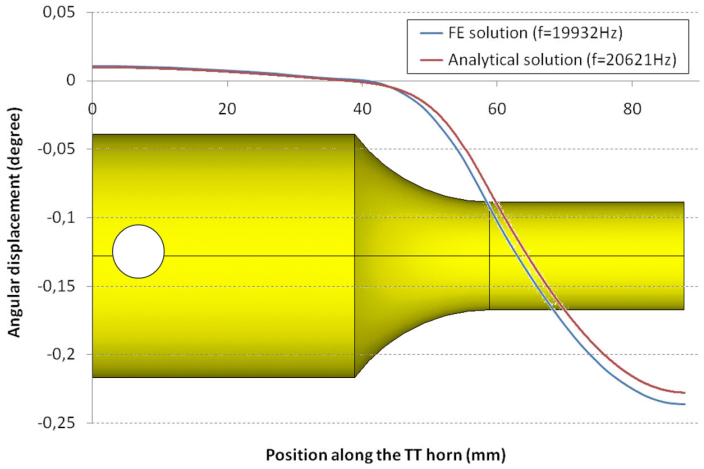

(b) TT Horn

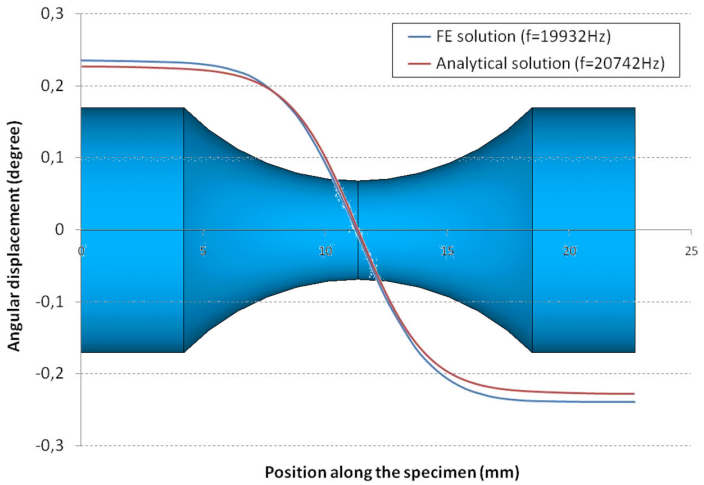

(c) Specimen

Figure 6: Amplitude of the longitudinal or angular displacement for each part using analytical and FEM approach.

frequency (f) of about 800 Hz ($\approx 4\%$). It can be observed that the displacement profiles evolve in the same way in the two analysis. The only difference is the amplitude at each end, which comes from the amplitude difference introduced by the previous parts of the system. This amplitude difference between both analysis is 4.4%. A small asymmetry can be also noticed on the amplitude of the angular displacement with respect to the specimen center for the FE model. This comes from the unavoidable non symmetry of the FE model with respect to the center of the specimen and the small difference on resonant frequency of each part. In terms of stress, the maximum shear stress amplitude reached in the center of the specimen is found to be 232.9 MPa for the FE model and 230.1 MPa for the 1D analytical solution, presenting a relative difference lower than 1.%.

It can be concluded that 1D analytical model returns a small difference on shear stress amplitude in the specimen with respect to the FE model, and could be considered for the development of a gigacycle indirect torsion fatigue system. But it is unable to help for the design of the connection between the two horns for which global FE model must be addressed.

5. Experimental validation and discrepancy assessment with theoretical models

5.1. Calibration and shear strain measurement

As seen previously, the calibration of the VHCF system relates the generator input voltage to the specific value of the input displacement and therefore, to the desired shear stress amplitude at the specimen surface, depending on the magnification factor. The calibration curves of the former and the optimised systems are plotted in Fig. 7. Calibration is done with a 100CrMo6 steel specimen showing a dynamic modulus of 210 GPa (same value as for numerical and anlytical analysis). The specimen is equipped with a strain gauge to determine the experimental shear strain, then the elastic shear stress is deduced. It can be observed that the relationship between the input voltage and the maximum shear stress amplitude is linear for both systems. It is clear that the magnification factor has been greatly increased for the optimised torsion fatigue system (by a factor of about 2 according to the results Tab. 5).

Moreover, since the maximum input voltage is 10 V, the optimised system should be theoretically suitable for high strength materials with torsion fatigue strength over 1000 MPa. The magnification factor obtained by the FE model is about 233 $MPa/\mu m$. It should be equal to the slope of the calibration curve by considering the input displacement of the TC horn in abscissa. This input displacement is measured by an optical fiber and the matching with the input voltage is found to be 0.387 $\mu m/V$. Consequently, the experimental magnification factor is equal to 132 $MPa/\mu m$. This one is around 43% lower than the numerical one.

This gap is important and can be related to: (i) experimental set-up (error in the experimental measurement by optical fibre and strain gauge, geometric imperfections due to machining, material properties which are not perfectly known, ...) and/or (ii) FE model and mainly contact conditions which are not considered.

Furthermore, these points can also explain the small difference on the resonant frequency between the FE model (19932 Hz) and the experimental system (20230 Hz), which is lower than 1.5%. In the next subsections, errors related to experimental measurements by strain gauge and to contact conditions in the FE model are discussed.

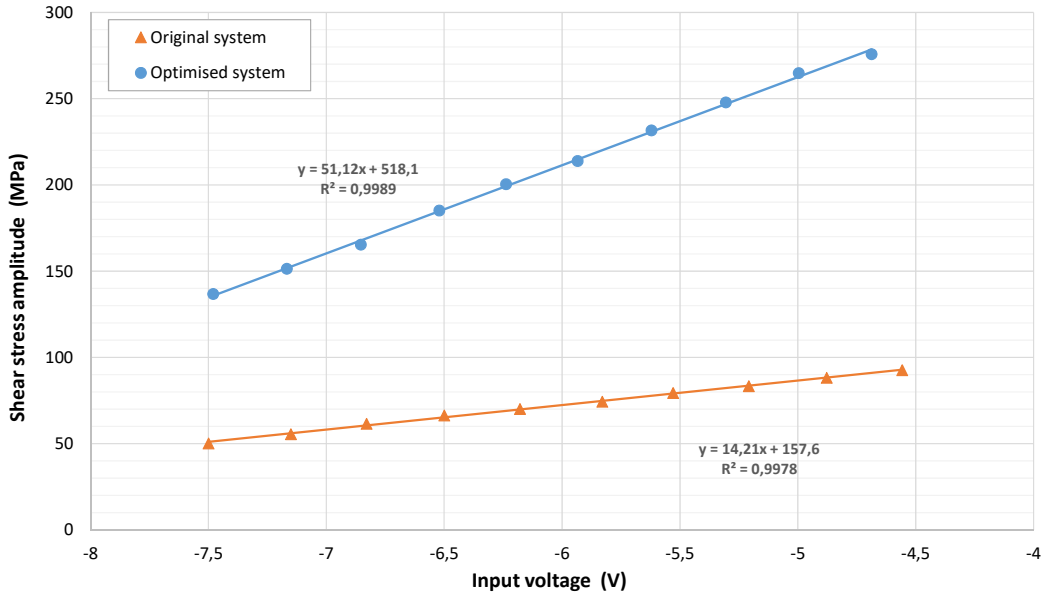

Figure 7: Calibration of the original and the optimised systems using the same steel specimen.

It can be noticed that the rather high difference between the experimental and the numerical magnification factors does not compromise the performances of the optimised system, because the 10 V maximum input voltage allows a more than 1000 MPa shear stress amplitude to be reached (see the linear relationship of the curve related the optimised system Fig. 7), convenient for a large range of materials, in particular with high torsion fatigue strength. In addition, for very high strength materials, a similar study on the specimen optimisation could be carried out.

5.2. Average value from strain gauge

The size of the gauge, which is not a point, can contribute to the deviation observed between results from numerical/analytical model and the real system. Indeed, the grid size of the gauge used to determine the experimental stress was around $3mm$ (a KIOWA KFG-2-120-C15-11 shear strain gauge was stuck on the specimen) and it can be remarked on Fig. 8 that the shear stress, calculated by numerical and analytic approaches with an imposed displacement of 1 μm on the TC horn, is not constant along the gauge. An average shear stress value of $217.2MPa$ is obtained along the gauge. Compared to the maximum value of $232.9MPa$, the discrepancy is near 7%.

5.3. Numerical modeling of contact conditions

This section is dedicated to the analysis of the difference between numerical and experimental results observed in the previous section. Harmonic analysis does not allow to introduce contact conditions as it is a linear analysis, therefore, we will discuss the introduction of contact conditions between the two horns and the pin using static and transient analysis.

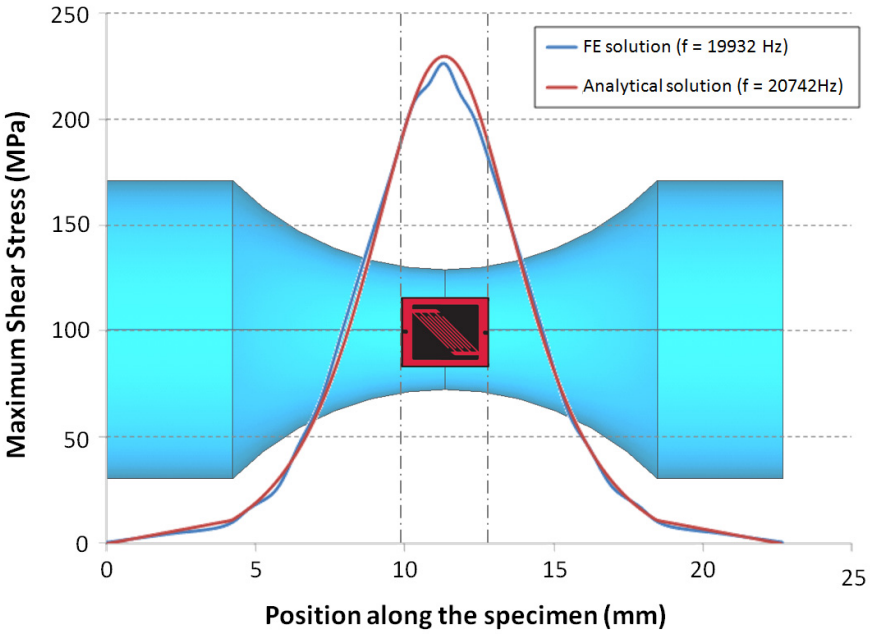

Figure 8: Maximum shear stress profile along the specimen for an imposed displacement of 1 μm on the TC horn and position of the strain gauge.

5.3.1. Static analysis

In this first section, a static analysis of the system is considered and compared with (i) a perfect model where the nodes of the two surfaces in contact between horns and pin are merged, and (ii) the introduction of natural contact conditions in a contact model. Fig. 9(a) presents the geometrical model considering two horns and the pin.

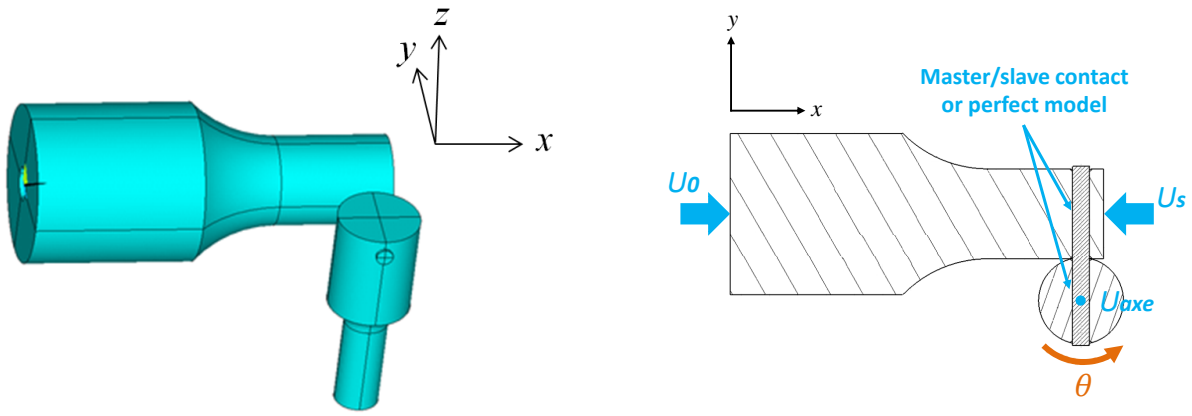

(a) 3D model

(b) boundary conditions

Figure 9: Geometry of the model and boundary conditions used for the static analysis.

The finite element model is described as follow:

Geometry: presented in Fig. 9(a), considering the real dimensions for the horns and the pin.

Finite element: Solid 186 in ANSYS® software.

angular displacement perfect model	angular displacement contact model	relative difference
0.568	0.456	24.6%

Table 6: Static analysis: angular displacement (in degree) at the free end of the pin.

Material properties: horns are in titanium alloy (TA6V) and pin is in 100CrMo6 quenched and tempered steel.

Boundary conditions: displacements along the $x-$axis ($U_0 = 3\ \mu m, U_s = -8.99\ \mu m$, with U_0 the amplitude of the vibration imposed by the piezo-electric converter, and U_s the amplitude of the vibration at the output of the horn) are introduced at the two ends of the tension-compression horn, corresponding, in one hand, to the experimental boundary condition imposed as the input of the system by the converter (left side of the TC horn in Fig. 9(a)) and, in other hand, to the amplified longitudinal displacement measured at the other end of the TC horn (its right side in Fig. 9(a)); straight line corresponding to the revolution axis of the TT horn along the z-axis is fixed ($U_{axis} = 0\ \mu m$) as it is considered to be the rotation axis of the torsion horn, see Fig. 9(b).

Contact condition: a classical friction coefficient between metallic materials $\mu = 0.2$ is arbitrarily introduced although the real friction coefficient between titanium and steel parts could be higher [29]. Then, comparison is made with a model in which all the nodes belonging to the interfaces between horns and pin are merged, called "perfect model".

Results: the angular displacement, denoted by θ, see Fig. 9(b), is considered as the output of the model.

The results are presented in Tab. 6. It can be observed that the influence of the contact conditions is important, regarding the angular displacement at the end of the pin. A 24.6% drop with respect to the perfect model is found.

5.3.2. Transient analysis

In this section, dynamic effects are taken into account to complete the static analysis of the previous section. The natural way to capture the dynamic effects in the case of sinusoidal cyclic loading is to performed an harmonic analysis. However, as said previously, contact conditions require a non-linear analysis incompatible with harmonic analysis, as a linear analysis. On the contrary, transient analysis with contact conditions is allowed in FE softwares such as ANSYS®, but it is not possible to simulate the whole experimental set-up because the computing time is prohibitive with this implicit FE software. Therefore a simpler two-dimensional axisymmetric model representing the pin inside a part of horn is considered for this transient analysis and comparison is made between a perfect model and a contact one, as before for static analysis. Fig. 10 shows the axisymmetric finite element model considering a line contact between an inner and an outer cylinders. A sinusoidal load of the form $U_0(t) = u_0 \sin(2\pi f t)$ with $f = 20\ kHz$ is imposed and the transient response is analysed. This simpler model is

not intended to represent the real system. It is used to roughly evaluate the effect of contact on the dynamic behavior of the assembly: pin + horn. Although in the real case, the direction of the vibrations is perpendicular to the pin, the work of the contact between the two parts is essentially done along the axis of the pin (because of shear at the pin-horn interface), hence the direction of displacement U_0 parallel to the inner cylinder axis (Fig. 10).

The finite element model is described as follow:

Geometry: axisymmetric two dimensional model (see Fig. 10), with length $L = 129\ mm$ and same value $l = 10\ mm$ for the width of the outer cylinder and radius of the inner one.

Finite element: Plane 42 in ANSYS® software.

Material properties: steel material.

Boundary condition: a sinusoidal displacement with amplitude $u_0 = 3\ mm$ at $20\ kHz$ (resonant frequency of the system) is applied at one end of the inner cylinder.

Contact condition: a classical friction coefficient $\mu = 0.2$ as explained in the previous section is introduced along the interface of the two cylinders and comparisons are proposed with the perfect model, where the nodes are merged.

Results: the displacement of the outer cylinder U_s, see Fig. 10, is considered as the output of the model.

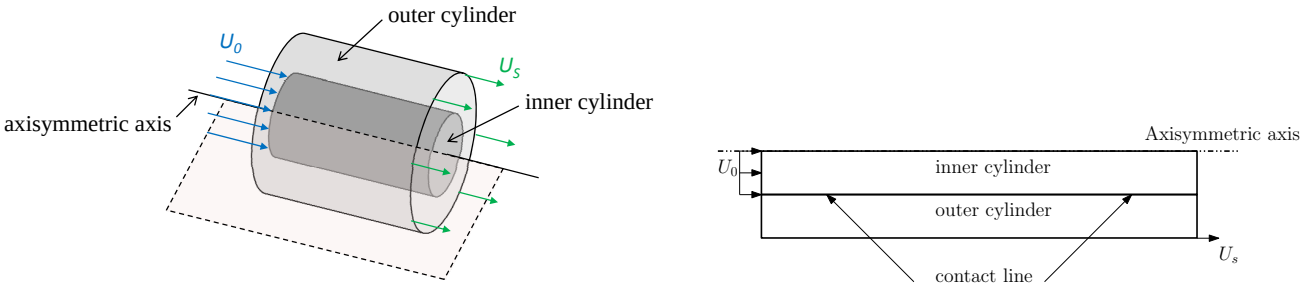

Figure 10: Transient analysis: 3D problem (left); geometry and boundary conditions for the axisymmetric FE model (right).

Fig. 11(a) presents the transient response of the perfect model (merged nodes) where the imposed displacement U_0 is in blue and the output displacement U_S is in green. The result is symmetric and the steady state value is 2.9 μm for U_s. A validation of the model is performed in the case "without contact" by comparing the transient response with the harmonic analysis, Fig. 11(b), where the steady state value of the perfect model is recovered. Fig. 11(c) shows the results for the contact model with the same color for input and output displacements as in Fig. 11(a). The steady state displacement value for U_s is 1.95 μm. Thus, the difference between perfect model and contact model is 48.7%, which is a high value compared to static analysis.

Consequently, in this section, simplified numerical models are considered for static and transient analysis using ANSYS® software in order to evaluate the effect of contact between solids. Tab. 7 shows the errors due to contact conditions for the considered models with respect to perfect models based on merged nodes. A wide range

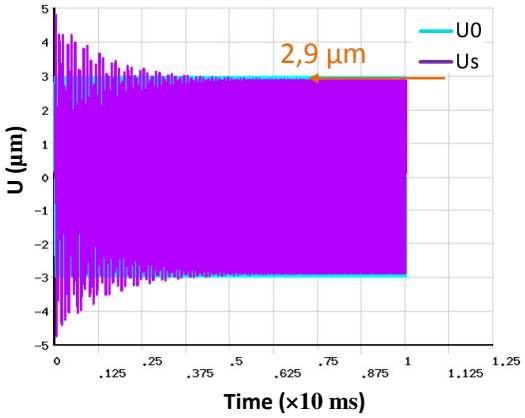

(a) Perfect model

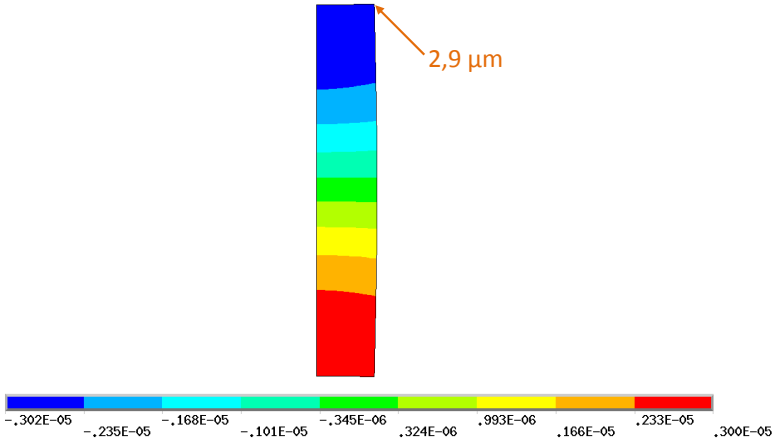

(b) Harmonic Analysis.

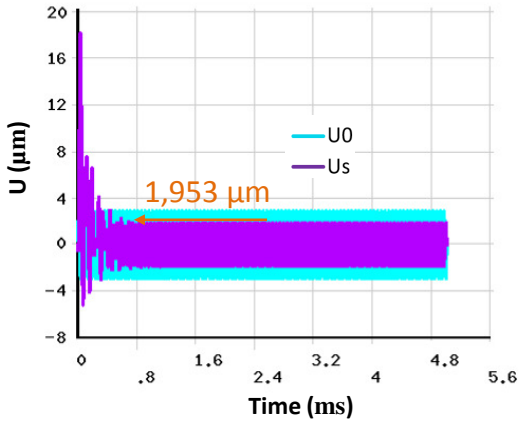

(c) Contact model

Figure 11: Transient and harmonic analysis: displacement results.

of error is obtained, varying from 25% to 49% and it could be inferred that the discrepancy between numerical models and experimental results for the whole system of the previous section is mainly related to the lack of contact conditions between horns and pin in the harmonic model.

model	relative difference
static	24.6%
transient	48.7%

Table 7: Static and transient analysis: relative difference between perfect model and contact model.

The last section of this paper is dedicated to ultrasonic fatigue tests on high strength steels in the gigacycle regime using the new experimental set-up reported in this paper.

6. Gigacycle fatigue tests on high strength steels

The evaluation of the performance of the optimised system from a numerical point of view was carried out in the last section. Now, the fatigue strength at 10^8 cycles under torsion ($R_\sigma = -1$) for the high strength steels 50CrV4 and 16MnCr5 are determined by the stair-case method [30] and observations of the fracture surfaces are then presented to confirm crack initiation under shear stress.

6.1. Materials and fatigue tests

The two materials tested for the validation of the new optimised ultrasonic torsion fatigue system are two high strength steels used in automotive industry. Their chemical composition and mechanical properties are given in Tab. 8 and Tab. 9 respectively. In this latter, E_d represents the dynamic Young modulus, ρ the density, σ_Y the yield stress, UTS the ultimate tensile strength, A the strain to fracture and HV the Vickers hardness. The 50CrV4 is a spring steel, quenched from austenitisation at 850°C during 30 minutes and tempered at 500°C during 1h. The obtained microstructure is tempered-martensite. Given the small size of the specimens, microstructure and mechanical properties are identical throughout the specimen cross section. The 16MnCr5 is a case of carburized steel grade. After carburization process, specimens were heated at 900°C and 860°C for 3h30 and 2h30 consecutively and then quenched in oil at 80°C and tempered at 160°C for 2 h. The obtained microstructure is martensite. The effect of the carburization highly strengthens the surface. The hardness gradually decreases until a depth of 1 mm. Note that the diameter at the center of the specimen is 4 mm. More details on these two materials are given in the final ERC project report [19].

	C	**Mn**	**Si**	**P**	**S**	**Cr**	**Ni**	**Mo**	**V**	**Cu**	**Al**	**Sn**	**Ti**	**N***
50CrV4	0.52	0.87	0.33	0.009	0.003	1.08	0.09	0.03	0.11	0.15	0.005	0.010	0.002	50
16MnCr5	0.16	1.10	0.27	0.011	0.021	1.02	0.11	0.03	0.01	0.14	0.021	0.009	0.002	110

Table 8: Chemical composition (in wt %) of the two steels (* in ppms).

The specimen geometry is shown in Fig. 12 and the modal analysis of this specimen gives a torsion natural frequency of 19785 Hz which is in good agreement with the resonance frequency of the whole system. For both

	E_d (GPa)	ρ (kg.m^{-3})	σ_Y (MPa)	UTS (MPa)	A (%)	HV
50CrV4	208.5	7871.0	1333	1409	13	310
16MnCr5	207.6	7796.6	867	1175	9.4	760/370 (surface/1 mm depth)

Table 9: Mechanical properties of the two steels.

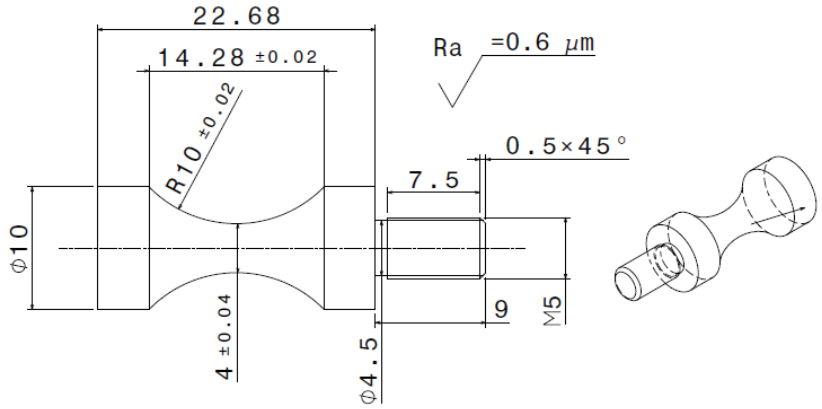

Figure 12: Design of the specimens for VHCF experimental campaign.

materials, the experimental magnification factor of the optimised ultrasonic torsion fatigue system was found to be $131 MPa/\mu m$.

Due to the important self-heating of these steels during ultrasonic tests, a continuous flow of water charged with inhibitor against corrosion is used to cool the specimens. The maximum shear stress amplitude imposed during this experimental campaign was 645 MPa, which is a higher value than the maximum value for the original system, but does not yet allow to evaluate the capacity of this new experimental set-up to test materials up to 1000 MPa. No very high strength material has been found yet to test the limits of the optimised torsion fatigue system.

The staircase method [28], based in this work on a set of 14 specimens per material, was applied to estimate the fatigue strength at 10^8 cycles. The results are 583.5 ± 6.5 MPa and 498.0 ± 12.6 MPa for 50CrV4 and 16MnCr5 respectively, where +/- indicates the standard deviation. Moreover, some specimens were tested until 10^9 cycles to build S-N curves in the VHCF domain. The results are presented in Fig. 13 for the two steels. It can be noticed that the shear stress amplitude is always higher for 50CrV4 than for 16MnCr5, although the S-N curve of the 50CrV4 decreases faster.

6.2. Fractography analysis of the specimens

Typical torsion fatigue cracks, as shown in Fig. 14(a) for 50CrV4 steel specimen, can be observed and a fractography is presented in Fig. 14(b) for 16MnCr5 steel specimen. As already reported in previous work [7], crack initiation occurs in mode II, resulting here in initiation perpendicular to the specimen axis, and then a bifurcation appears leading to a crack propagation in mode I according to a 45° angle with respect to

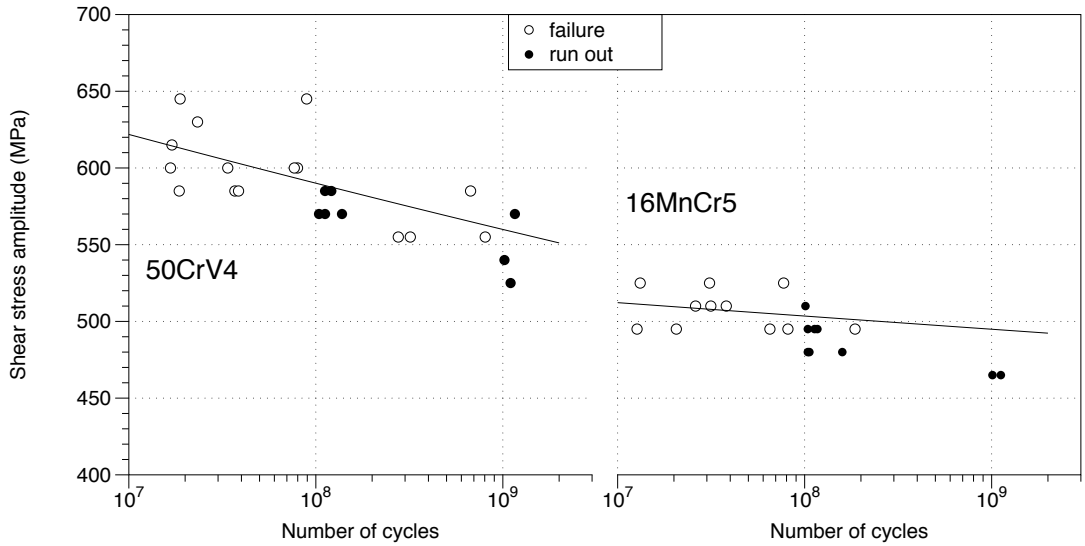

Figure 13: S-N curves under torsion (R = -1) for 50CrV4 and 16MnCr5 steels. Slopes don't take into account for the run out specimens.

the longitudinal specimen axis, before complete fracture. Indeed, after crack initiation, crack opening occurs perpendicularly to principal stresses, oriented at 45° from the specimen axis.

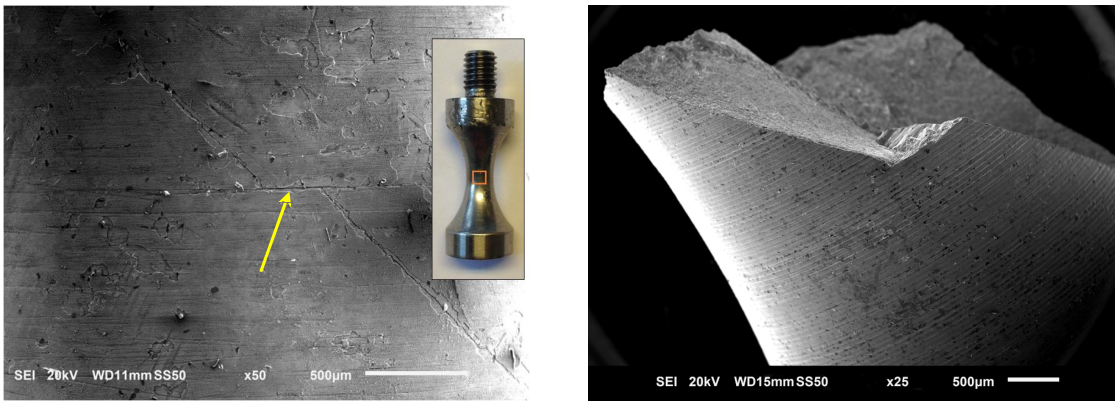

(a) Crack propagation in 50CrV4

(b) Fracture surface of 16MnCr5

Figure 14: Fractographic analysis of two high strength steel specimens: 50CrV4 and 16MnCr5. The arrow shows the shear crack initiation.

7. Conclusion and prospects

An optimised ultrasonic torsion fatigue system has been presented in this paper. The principle of this system is based on the indirect system designed by Bathias et al. [11], 15 years ago. The improved experimental set-up proposed in this paper was numerically optimised using static and harmonic FEM analysis. Four fundamental parameters were analysed through a parametric study: TT horn dimensions, pin size, chamfers along drilling edges and bore in horns. Each parameter was individually investigated and a final set of optimised parameters was chosen. The optimised system meets two objectives: increases the shear stress amplitude in the specimen

during ultrasonic torsion fatigue test, and decreases stresses in the system, in particular, in the pin part which links the two horns. This was the weak point which broke in the original system.

A discrepancy around 43% on the maximum shear stress in the specimen was observed between experimental and analytical/numerical results; the experimental value being the lower. This difference is explained by the fact that the contact conditions (non perfect) between parts is not taken into account in the analytical and numerical models. Two simplified numerical models for static and transient analysis were developped in order to highlight the importance of the contact conditions on the loss of energy in dynamics. The gap between experimental and numerical results shows that the experimental calibration using strain gauges of an ultrasonic fatigue system is essential, while a numerical model may not be sufficient.

Some experimental tests were performed on two high strength steel, allowing to validate the improved performances and robustness of this new experimental set-up. In [11], the maximum shear stress for ultrasonic fatigue tests on 38MnSV5S steel specimens was 260 MPa while in the present experimental campaign, up to 650 MPa was applied without any failure problem on the experimental set-up. Nevertheless, higher strength materials should be tested to assess the maximum stress level capability of the optimised system; it will be our future work.

Aknowlegdement

A part of this work has received funding from the European Union's Research Fund for Coal and Steel (RFCS) research programme under grant agreement n° RFS-CT-2013-00015 (FREQTIGUE). Sincere thanks to the project's partners: Karlstads Universitet, Centro Ricerche FIAT SCPA, Arcelor Mittal Maizieres Research SA, Karlsruher Institut für Technologie, Rheinisch-Westfaelische Technische Hochschule Aachen and Sidenor. A special thanks to Sidenor company for the steel specimens used in the last section of this paper.

Appendix A. Design of the specimen

In order to design the specimen for torsional resonant frequency in the range of $20kHz(\pm 500Hz)$, the methodology is shortly described below, using the geometric parameters defined in Fig. A.15. The radius of the cylindrical part is denoted by R_c and the one of the central section by R_m, where the maximum value of the transverse shear stress is reached. Furthermore, two lengths are defined, one for the cylindrical part, L_c, and one for the part with the progressive section, L_v.

The analysis is conducted on half of the specimen, using the symmetry of the geometry. The shape of the variable section is described by an hyperbolic cosinus function, allowing the analytical resolution of the differential equation of the movement given in the paragraph below.

Appendix A.1. Equations for wave propagation in torsion

The wave propagation in torsion is governed by the ordinary differential equation obtained by applying the principle of angular momentum on a differential element dz:

$$I_P(z)\frac{\partial^2\varphi}{\partial t^2} = G\frac{\partial}{\partial z}\left(J_T(z)\frac{\partial\varphi}{\partial z}\right)dz \tag{A.1}$$

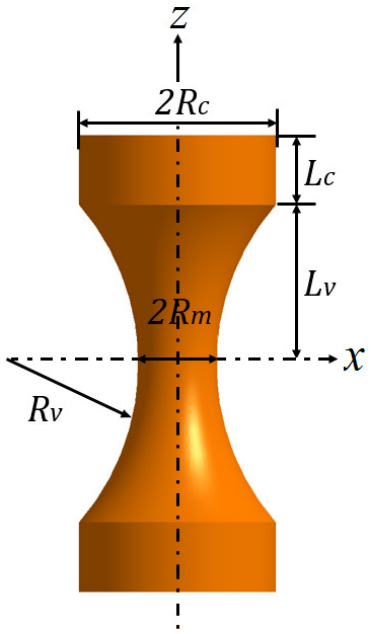

Figure A.15: Geometry and parameters for the specimen.

where:

– $\varphi = \varphi(z,t)$ is the torsion angle depending on (z,t)

– G is the dynamic transverse shear modulus of the material

– ρ is the volume mass

– $J_T(z)$ is the polar quadratic moment of a section related to z

– $I_P(z)$ is the moment of inertia around z of the section related to z

As the section is homogeneous, we have $I_P(z) = \rho J_T(z)\mathrm{d}z$, and I_P and J_T are assumed independent of time. For a cylindrical section $S(z)$ of radius $R(z)$, we recover

$$J_T(z) = \frac{\pi}{2}R^4(z) = \frac{S^2(z)}{2\pi} \tag{A.2}$$

and Eq. (A.1) can be simplified as

$$\frac{\partial^2\varphi(z,t)}{\partial t^2} - \frac{G}{\rho}\frac{\partial\varphi(z,t)}{\partial z}\frac{\mathrm{d}(\ln S^2(z))}{\mathrm{d}z} - \frac{G}{\rho}\frac{\partial^2\varphi(z,t)}{\partial z^2} = 0 \tag{A.3}$$

If the vibration is supposed to be sinusoidal, the torsion angle $\varphi(z,t)$ can be expressed as a function of the angular amplitude $\theta(z)$

$$\varphi(z,t) = \theta(z)e^{i\omega t} \tag{A.4}$$

Then Eq. (A.3) becomes

$$\frac{\mathrm{d}^2\theta(z)}{\mathrm{d}y^z} + \frac{\mathrm{d}(\ln S^2(z))}{\mathrm{d}z}\frac{\mathrm{d}\theta(z)}{\mathrm{d}z} + K^2\theta(z) = 0 \tag{A.5}$$

with

$$K = \frac{\omega}{c} \qquad c = \sqrt{\frac{G_d}{\rho}}$$

where:

– ω is the circular frequency, with $\omega = 2\pi f$

– c is the wave propagation velocity in the material

Eq. (A.5) allows to determine the rotation angle $\theta(z)$ of the section $S(z)$ for each z position along the specimen axis, but first, the geometric parameters corresponding to the resonant frequency have to be determined.

Appendix A.2. Determination of the geometric parameters

The section S is written with respect to z as follow :

$$S(z) = S_c \qquad L_v \leq |z| \leq L \tag{A.6}$$

$$S(z) = S_m \cosh(\alpha z) \qquad 0 \leq |z| \leq L_v \tag{A.7}$$

with

$$\alpha = \frac{1}{L_v} \text{arccosh}(\frac{S_c}{S_m}) \tag{A.8}$$

Solving Eq. (A.5) for the two parts of the half specimen (denoted I for the cylindrical and II for the variable part) gives two equations with two constants for each one. These unknowns are determined using

- the boundary conditions at the end of the cylindrical part

$$\begin{aligned} \theta_I(z) \mid_{z=-L} &= \theta_s \\ \theta'_I(z) \mid_{z=-L} &= 0 \end{aligned} \tag{A.9}$$

- the continuity conditions between the two parts

$$\theta_I(z) \mid_{z=-L_v} = \theta_{II}(z) \mid_{z=-L_v} \tag{A.10}$$

- the symmetry condition

$$\theta_{II}(z) \mid_{z=0} = 0 \tag{A.11}$$

Then, the rotation angle $\theta(z)$ along the specimen is deduced

$$\begin{aligned} \theta(z) &= \theta_s \cos[K(L-z)] \qquad L_v \leq |z| \leq L \\ \theta(z) &= \theta_s \psi(L_c, L_v) \frac{\sinh(\beta z)}{\cosh(\alpha z)} \qquad 0 \leq |z| \leq L_v \end{aligned} \tag{A.12}$$

where

$$\psi(L_c, L_v) = \frac{\cos(KL_c)\cosh(\alpha L_v)}{\sinh(\beta L_v)} \tag{A.13}$$

$$\beta = \sqrt{\alpha^2 - K^2} \tag{A.14}$$

The resonant length L_c is obtained as follow

$$L_c = \frac{1}{K}\arctan\left(\frac{1}{K}\left(\frac{\beta}{\tanh(\beta L_v)} - \alpha\tanh(\alpha L_v)\right)\right) \tag{A.15}$$

using the supplementary continuity condition

$$\theta'_I(z)\mid_{z=-L_v} = \theta'_{II}(z)\mid_{z=-L_v} \tag{A.16}$$

Appendix A.3. Determination of the maximal transverse shear stress

At the z position, the relation between the circumferential displacement $U(z)$ on the specimen perimeter and the rotation angle $\theta(z)$ is

$$U(z) = R(z)\,\theta(z) \tag{A.17}$$

Furthermore, the transverse shear stress $\tau(z)$ is deduced from the Hooke law and the transverse shear strain $\gamma(z)$ by

$$\tau(z) = G\,\gamma(z) = G\,R(z)\,\frac{\mathrm{d}\theta(z)}{\mathrm{d}z} \tag{A.18}$$

From Eq. (A.12) and Eq. (A.18), the transverse shear stress can be deduced in the specimen

- for the cylindrical part with $L_v \leq |z| \leq L$

$$\begin{aligned} U(z) &= R_c\theta_s\cos[K(L-z)] \\ \gamma(z) &= R_c\theta_s K\sin[K(L-z)] \\ \tau(z) &= G\gamma(z) \end{aligned} \tag{A.19}$$

- for the variable part with $0 \leq |z| \leq L_v$

$$\begin{aligned} U(z) &= R_m\theta_s\psi(L_c,L_v)\frac{\sinh(\beta z)}{\sqrt{\cosh(\alpha z)}} \\ \gamma(z) &= \psi(L_c,L_v)R_m\theta_s\frac{\sqrt{\cosh(\alpha z)}[\beta\cosh(\beta z)\cosh(\alpha z) - \alpha\sinh(\beta z)\sinh(\alpha z)]}{\cosh^2(\alpha z)} \\ \tau(z) &= G\gamma(z) \end{aligned} \tag{A.20}$$

Therefore, the maximum transverse shear stress is deduced for the central section of the specimen at $z = 0$:

$$\tau_{max} = G\psi(L_c,L_v)R_m\theta_s\beta \tag{A.21}$$

References

[1] C. Bathias, There is no infinite fatigue life in metallic materials, Fatigue Fracture Engineering Materials Structures 22 (1999) 559–565.

[2] W. P. Mason, Use of high amplitude strains in studying wear and ultrasonic fatigue in metals., in: J. Well, O. Buck Roth, J. Tien (Eds.), Ultrasonic fatigue, proceedings of the first international conference on fatigue and corrosion fatigue up to ultrasonic frequencies, The Metallurgical Society of AIME, 1982, pp. 87–102.

[3] S. E. Stanzl, H. R. Mayer, E. K. Tschegg, High frequency method for torsion fatigue testing, Ultrasonics 31 (4) (1993) 275–280.

[4] C. Bathias, Piezoelectric fatigue testing machines and devices, International Journal of Fatigue 28 (11) (2006) 1438 – 1445.

[5] Y. Shimamura, K. Narita, H. Ishii, K. Tohgo, T. Fujii, T. Yagasaki, M. Harada, Very high cycle fatigue properties of carburized steel by ultrasonic torsional fatigue testing, Journal of the Society of Materials Science 59 (2) (2010) 938–943.

[6] G. Pisarenko, P. Kul'bashny, High-frequency fatigue testing machine with quarter-wave magnetostrictive vibrator, Strength Mater 1 (1969) 428–429.

[7] E. Bayraktar, C. Bathias, H. Q. Xue, H. Tao, On the gigacycle fatigue behaviour of two-phase $(\alpha_2 + \gamma)$ tial alloy, International Journal of Fatigue 26 (12) (2004) 1263–1275.

[8] H. Ishii, T. Yamada, Y. Okada, Very high cycle fatigue strengths of thin sheet metals, in: 3rd International conference on very high cycle fatigue (VHCF-3), Shiga and Kyoto, Japan, 2004, pp. 420–426.

[9] P. F. Filgueiras, C. Bathias, E. S. Palma, C. Wang, Inducing very high cycle fretting-fatigue in the ultrasonic regime, Tribology International 76 (2014) 57–62.

[10] H. Mayer, Ultrasonic torsion and tension–compression fatigue testing: Measuring principles and investigations on 2024-t351 aluminium alloy, International Journal of Fatigue 28 (11) (2006) 1446 – 1455.

[11] I. Marines-Garcia, J.-P. Doucet, C. Bathias, Development of a new device to perform torsional ultrasonic fatigue testing, International Journal of Fatigue 29 (9–11) (2007) 2094 – 2101.

[12] N. Sakanaka, Y. Matsubara, Y. Shimamura, H. Ishii, Rapid evaluation of shear fatigue properties of rolling bearing steels for lifespans up to the gigacycle range, NTN Technical Review 79 (2011) 104–110.

[13] H. Mayer, R. Schuller, U. Karr, D. Irrasch, M. Fitzka, M. Hahn, M. Bacher-Höchst, Cyclic torsion very high cycle fatigue of {VDSiCr} spring steel at different load ratios, International Journal of Fatigue 70 (2015) 322 – 327.

[14] A. Nikitin, C. Bathias, T. Palin-Luc, A new piezoelectric fatigue testing machine in pure torsion for ultrasonic gigacycle fatigue tests: application to forged and extruded titanium alloy, Fatigue Fracture Engineering Materials Structures 38 (2015) 1294–1304.

[15] S. E. Stanzl, M. Czegley, H. R. Mayer, E. K. Tschegg, Fatigue crack growth under combined mode i and mode ii loading, in: R. Wei, R. Gangloff (Eds.), Fracture mechanics: perspectives and directions, Vol. 31, ASTM STP 1020, Philadelphia, 1989, pp. 479–496.

[16] E. K. Tschegg, H. R. Mayer, M. Czegley, S. E. Stanzl, Influence of a constant mode III load on mode I fatigue crack growth thresholds, in: K. Kussmaul, D. McDiarmid, D. Socie (Eds.), Fatigue under biaxial and multiaxial loading, Vol. 10 of Mechanical Engineering Publications, ESIS, London, 1991, pp. 213–222.

[17] P. Costa, M. Vieira, L. Reis, A. Ribeiro, M. de Freitas, New specimen and horn design for combined tension and torsion ultrasonic fatigue testing in the very high cycle fatigue regime, International Journal of Fatigue 103 (2017) 248–257.

[18] M. Fitzka, H. Mayer, Constant and variable amplitude fatigue testing of aluminum alloy 2024-t351 with ultrasonic and servo-hydraulic equipment, International Journal of Fatigue 91 (2) (2015) 363–372.

[19] J. Bergstrom, et al., Influence of cycling frequency on fatigue strength and crack growth of engineering steels for demanding applications, Freqtigue project, Final Technical Report RFS-CT-2013-00015, European Commission: Research Programme of the Research Fund for Coal and Steel (2017).

[20] Y. Akiniwa, S. E. Stanzl-Tschegg, H. Mayer, M. Wakita, K. Tanaka, Fatigue strength of spring steel under axial and torsional loading in the very high cycle regime, International Journal of Fatigue 30 (2008) 2057–2063.

[21] Y. Shimamura, K. Narita, H. Ishii, K. Tohgo, T. Fujii, T. Yagasaki, M. Harada, Fatigue properties of carburized alloy steel in very high cycle regime under torsional loading, International Journal of Fatigue 60 (2014) 57–62.

[22] A. Nikitin, T. Palin-Luc, A. Shanyavskiy, C. Bathias, Comparison of crack paths in a forged and extruded aeronautical titanium alloy loaded in torsion in the gigacycle fatigue regime, Engineering Fracture Mechanics 167 (2016) 259–272.

[23] H. Q. Xue, E. Bayraktar, I. Marines-Garcia, C. Bathias, Torsional fatigue behaviour in gigacycle regime and damage mechanism of the perlitic steel, Journal of Achievements in Materials and Manufacturing Engineering 31 (2) (2008) 391–397.

[24] E. Mori, M. Uno, Analysis of torsional vibration of an ultrasonic exponential solid horn with a tool and its design considering fatigue limit, in: Bulletin Tokyo Institute of Technology, Vol. 51, TIT, 1963, pp. 63–80.

[25] H. Q. Xue, Explanation on gigacycle fatigue of materials in tension, bending and torsion loading, Ph.D. thesis, CNAM, Arts et Metiers (2005).

[26] A. Nikitin, Gigacycle fatigue of a titane alloy, Ph.D. thesis, University of Paris Nanterre (2015).

[27] Z. Jiang, Développement d'une machine de fatigue gigacyclique en torsion pour les matériaux métalliques à haute résistance, Ph.D. thesis, University of Paris Nanterre (2017).

[28] C. Bathias, P. C. Paris, Gigacycle Fatigue in Mechanical Practice, Vol. 22, CRC Press, 2004.

[29] J. Qu, P. J. Blau, T. R. Watkins, O. B. Cavin, N. S. Kulkarni, Friction and wear of titanium alloys sliding against metal, polymer, and ceramic counterfaces, Wear 258 (2005) 1348 – 1356.

[30] W. J. Dixon, A. M. Mood, A method for obtaining and analysing sensitivity data, Journal of the American Statistical Association 43 (1948) 109–126.